Volume 13
Number 7
21 February 2025
Pages 2215–2562

Journal of Materials Chemistry B

Materials for biology and medicine

rsc.li/materials-b

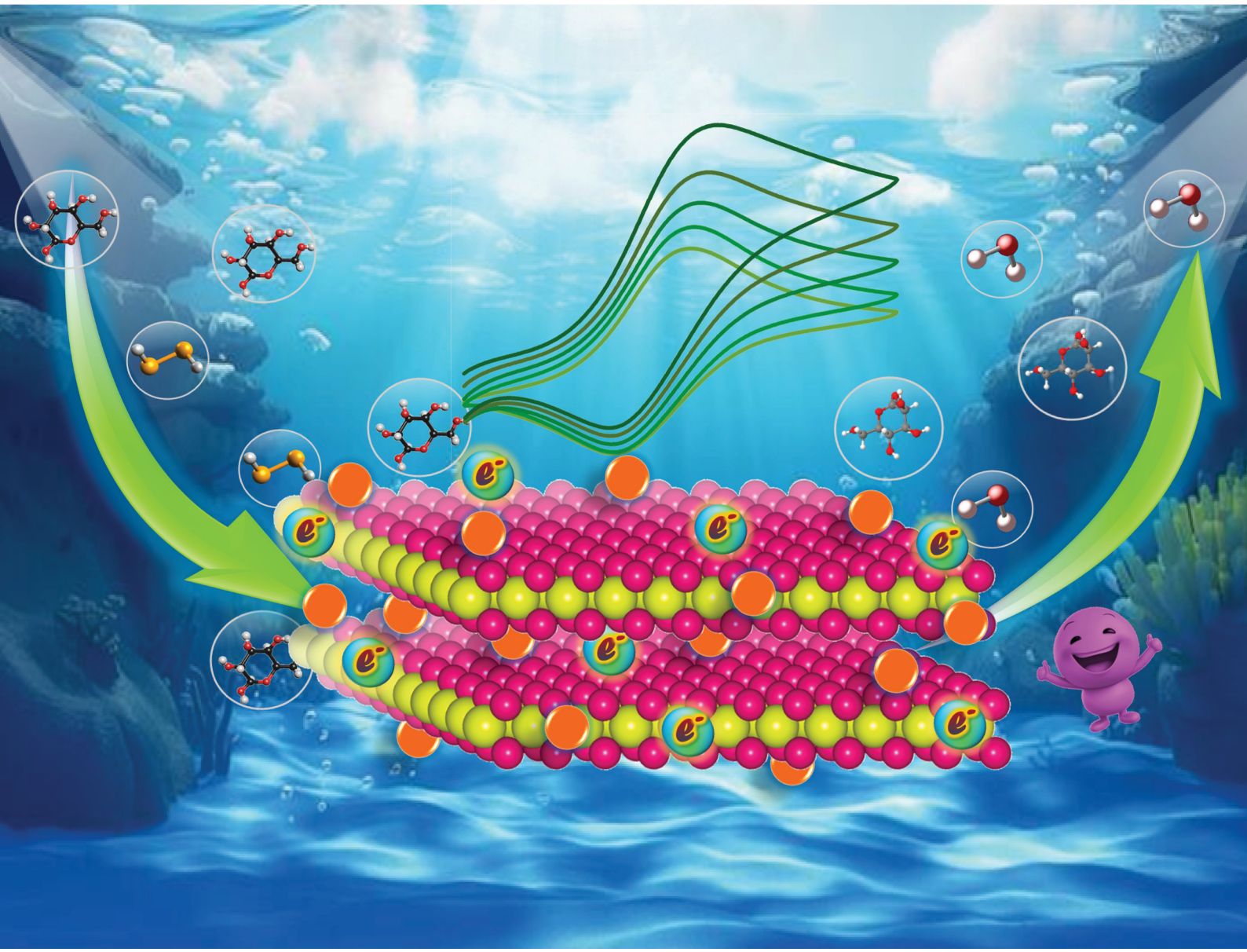

ISSN 2050-750X

ROYAL SOCIETY OF CHEMISTRY

PAPER

Devarasu Mohanapriya and Kathavarayan Thenmozhi
In situ developed $NiCo_2O_4$–$Ti_3C_2T_x$ nanohybrid towards non-enzymatic electrochemical detection of glucose and hydrogen peroxide

Journal of Materials Chemistry B

ROYAL SOCIETY OF CHEMISTRY

PAPER

View Article Online
View Journal | View Issue

Cite this: J. Mater. Chem. B, 2025, 13, 2306

In situ developed $NiCo_2O_4$–$Ti_3C_2T_x$ nanohybrid towards non-enzymatic electrochemical detection of glucose and hydrogen peroxide†

Devarasu Mohanapriya and Kathavarayan Thenmozhi *

Owing to the adverse consequences of excess glucose (Glu) and hydrogen peroxide (H_2O_2) on humans, it is imperative to develop an electrochemical sensor for detection of these analytes with good selectivity and sensitivity. Herein, a nanohybrid comprising nickel cobaltite nanoparticles ($NiCo_2O_4$ NPs) embedded on conductive $Ti_3C_2T_x$ nanosheets (NSs) has been prudently designed and employed for the electrochemical detection of Glu and H_2O_2. The developed nanohybrid has been systematically characterized using morphological and spectral techniques, and then immobilized on a glassy carbon electrode (GCE). Under optimized conditions, the developed $NiCo_2O_4$–$Ti_3C_2T_x$/GCE based electrochemical sensor has demonstrated an impressive analytical response towards Glu and H_2O_2 with good sensitivity and selectivity. The non-enzymatic sensor has demonstrated a broad linear range from 30 μM to 1.83 mM for Glu, and two linear ranges of 20–100 μM and 100 μM–2.01 mM for H_2O_2. The sensor has exhibited limits of detection (LOD) of 9 μM and 6 μM with sensitivities of 101.2 μA μM^{-1} cm^{-2} and 107.03 μA μM^{-1} cm^{-2}, respectively, for Glu and H_2O_2 detection. The impressive analytical performance of the fabricated sensor in terms of linear range, LOD and sensitivity are ascribed to the (i) enhanced conductivity of $Ti_3C_2T_x$ NSs, (ii) mediated electrocatalytic activity of $NiCo_2O_4$ NPs and (iii) large number of catalytically active sites on the $NiCo_2O_4$–$Ti_3C_2T_x$ heterostructure. Notably, the $NiCo_2O_4$–$Ti_3C_2T_x$/GCE has demonstrated impressive stability and reproducibility, which is mainly due to the *in situ* uniform growth of $NiCo_2O_4$ NPs over $Ti_3C_2T_x$ NSs.

Received 8th October 2024,
Accepted 8th December 2024

DOI: 10.1039/d4tb02265c

rsc.li/materials-b

1. Introduction

The design and fabrication of extremely specific and precise diagnostic devices that can be used in analytical assays, and in particular identification of biomolecules, are crucial for the sustainability of human life and the environment. Glucose (Glu) and hydrogen peroxide (H_2O_2) are the most investigated analytes and excessive concentrations of these molecules in bodily fluids can have adverse impacts on human health.[1–3] The Glu level in the human body is regarded as a pathological indicator of diabetes and an increase in blood sugar level causes chronic microvascular problems in diabetes patients.[4,5] Therefore, rapid, reliable and everyday monitoring of Glu in blood is extremely beneficial for the early identification and treatment of diabetes and related ailments.[6–8] Similarly, H_2O_2 is one of the most significant biomarkers of oxidative stress and also serves as a precursor to extremely reactive and possibly hazardous hydroxyl radical formation.[9] Anomalous H_2O_2 concentrations in both plasma and cells have been associated with a number of illnesses, including cerebrovascular dysfunction and cancer, and can cause gene mutation and DNA damage.[10–12] Hence, researchers are continuously exploring quick and sensitive techniques towards the quantitative determination of H_2O_2 and Glu for clinical diagnosis.

Electrochemical sensors have attracted significant attention among various analytical techniques because of their numerous advantages, including high sensitivity, simplicity, low cost, high throughput, fast operation and the potential for miniaturization.[13–15] The effectiveness of electrochemical sensors depends on the properties of the sensing element, typically an electrode modifier. Initially, enzyme-based materials were utilized as a sensing element for selective and sensitive detection of a targeted analyte.[16] Conversely, there are a few disadvantages associated with enzyme-based sensors, which

Department of Chemistry, School of Advanced Sciences, Vellore Institute of Technology (VIT), Vellore-632014, India. E-mail: kt.thenmozhi@gmail.com, k.thenmozhi@vit.ac.in

† Electronic supplementary information (ESI) available: Materials, instrumentation, XRD patterns of Ti_3AlC_2 and $Ti_3C_2T_x$ NS, FESEM image of Ti_3AlC_2, $Ti_3C_2T_x$ NSs, $NiCo_2O_4$ NPs and $NiCo_2O_4$–$Ti_3C_2T_x$ nanohybrid, FESEM image and elemental analysis of the $NiCo_2O_4$–$Ti_3C_2T_x$ nanohybrid, Effect of pH, effect of scan rate and corresponding calibration plot, Real time detection of Glu and H_2O_2, comparison table of $NiCo_2O_4$–$Ti_3C_2T_x$/GCE sensor with previously reported Glu and H_2O_2 sensors. See DOI: https://doi.org/10.1039/d4tb02265c

include the difficulties in modification, instability and tedious immobilization processes.[17,18]

Consequently, non-enzymatic sensors, especially those based on transition metal oxides, have attracted much interest and are becoming a replacement for enzymatic sensors.[19] Among the different metal oxides, transition metal spinel cobaltites (MCo_2O_4) exhibit excellent electrocatalytic activity compared to monometallic oxides.[20] Recently, various spinel cobaltites have been reported, among which nickel cobaltite ($NiCo_2O_4$) has been explored to a great extent due to its ease of synthesis, affordability, biocompatibility, strong ionic conductivity, and exceptional electrochemical activity.[21,22] The synergetic effect between the two metals could modulate the electronic structure of $NiCo_2O_4$ NPs, which in turn would enhance its electrocatalytic properties. The efficacy of $NiCo_2O_4$ could still be enhanced by converting it to a nano-sized material and uniformly embedding it over appropriate supports. This strategy would offer enough anchoring sites to properly immobilize the NPs and prevent their overgrowth. Different conductive supports such as graphene oxides (GO), MXene, multi-walled carbon nanotubes (MWCNTs) and graphitic carbon nitride (gC_3N_4) could be employed for the growth of $NiCo_2O_4$ NPs in order to increase the electrocatalytic efficiency and stability.[23–25]

Recently, (2D) single-layer MXene has been established as a promising material in electrochemical sensing. Titanium carbide MXene ($Ti_3C_2T_x$) is one of the heavily investigated 2D MXenes by virtue of its distinct characteristics, including high conductivity, large surface area, remarkable electrochemical stability and abundant functional groups (relative to other synthesized MXenes).[26–29] Interestingly, the terminal groups, such as –O, –OH, –F, and –Cl, on the surface of $Ti_3C_2T_x$ NSs could serve as growth sites for the dispersion and stabilisation of metal oxide NPs.[30,31] MXenes and $NiCo_2O_4$ materials have been individually utilized for various applications in the past, whereas limited research has been devoted towards their combined functionalities. This motivated us to develop a nanostructure comprising $NiCo_2O_4$ NPs and $Ti_3C_2T_x$ NSs to trigger the catalytically active sites and further to employ it for the electrochemical detection of biomolecules. To the best of our knowledge, the combination of a $NiCo_2O_4$ NPs decorated $Ti_3C_2T_x$ MXene based nanohybrid has not been probed for the detection of both Glu and H_2O_2. With the aforementioned background, a robust non-enzymatic sensor has been constructed in this work, utilizing a $NiCo_2O_4$ NPs decorated $Ti_3C_2T_x$ NSs modified GCE for Glu and H_2O_2 sensing. In the sensor setup, MXene provides an active surface towards the uniform growth of $NiCo_2O_4$ NPs and the *in situ* growth prevents the agglomeration of NPs. The prepared nanohybrid was thoroughly characterized using different morphological and spectral investigations. The developed sensor exhibited outstanding selectivity and sensitivity towards Glu oxidation and H_2O_2 reduction. Additionally, the fabricated sensor was employed to detect the targeted analyte in food, serum and urine samples, where it displayed impressive recoveries.

2. Experimental

All chemicals and instrumentation details are given in the ESI.†

2.1. Synthesis of $Ti_3C_2T_x$ NSs

$Ti_3C_2T_x$ NSs were synthesized by selective etching of the Al layer from readily available bulk MAX phase Ti_3AlC_2 MAX, using an *in situ* HF etching method[32] (Fig. 1). Briefly, 2 g of LiF was added to 40 mL of HCl (9 M) with rapid stirring, and then 2 g of Ti_3AlC_2 powder was slowly added to the above solution to avoid overheating. Subsequently, Al etching was carried out over 24 h with continuous stirring of the aforementioned solution at 35 °C. The obtained suspension was subjected to washing several times using deionized water and centrifuged until the pH of the solution reached 6. The obtained sediment was mixed with deionized water and sonicated for 1 h with continuous Ar bubbling. $Ti_3C_2T_x$ NSs were obtained after the solution was freeze-dried for 24 h at −50 °C.

2.2. Synthesis of the $NiCo_2O_4$–$Ti_3C_2T_x$ nanohybrid

To synthesize the proposed nanohybrid,[33] 10 mg of $Ti_3C_2T_x$ NSs were ultrasonically dispersed in deionized water (10 mL) for 1 h. Furthermore, 20 mmol and 40 mmol of cobalt(II) chloride hexahydrate and nickel(II) chloride hexahydrate were mixed in 25 mL of deionized water and poured into the above mentioned $Ti_3C_2T_x$ NS solution with stirring (30 min) to obtain a homogenously dispersed solution. This homogeneous solution was transferred into a 50 mL stainless steel autoclave for hydrothermal treatment and kept at 160 °C for 6 h. After the reaction was completed, the resulting product was repeatedly washed with deionized water and ethanol before being dried overnight in an oven at 80 °C. Finally, the synthesised material was calcined at 400 °C for about 3 h with a heating rate of 3 °C per minute to finally obtain the $NiCo_2O_4$–$Ti_3C_2T_x$ nanohybrid material (Fig. 1). The same synthesis method was followed to prepare $NiCo_2O_4$ without adding $Ti_3C_2T_x$.

2.3. Fabrication of the $NiCo_2O_4$–$Ti_3C_2T_x$ nanohybrid modified electrode

The GCE surface was successively polished before every electrode modification using 1, 0.3, and 0.05 μm sized alumina powder on

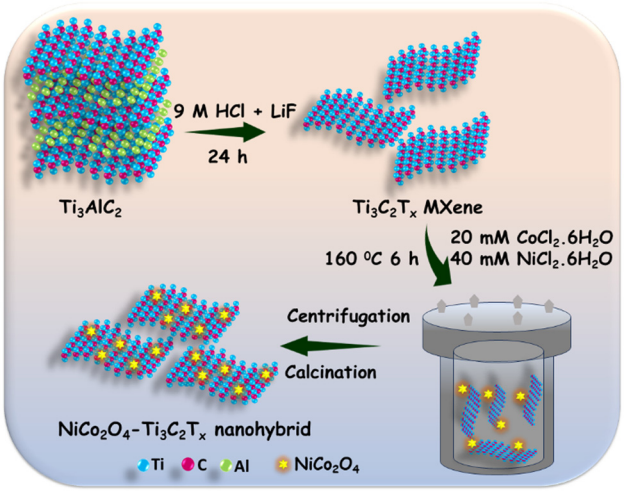

Fig. 1 Schematic representation for the preparation of the $NiCo_2O_4$–$Ti_3C_2T_x$ nanohybrid.

a leather polishing pad. The surface residues were then removed by ultrasonication in Milli-Q water and ethanol (1 : 1). The pre-cleaned GCE surface was then drop-casted with 10 μL of $NiCo_2O_4$–$Ti_3C_2T_x$ nanohybrid (2 mg mL^{-1}), and was air dried to obtain $NiCo_2O_4$–$Ti_3C_2T_x$/GCE. Similarly, $NiCo_2O_4$ NPs and $Ti_3C_2T_x$ NSs modified GCEs ($NiCo_2O_4$/GCE and $Ti_3C_2T_x$/GCE) were also prepared for comparison.

3. Results and discussion

3.1. Characterization of the $NiCo_2O_4$–$Ti_3C_2T_x$ nanohybrid

The PXRD patterns of Ti_3AlC_2, $Ti_3C_2T_x$ NSs, $NiCo_2O_4$ NPs and the $NiCo_2O_4$–$Ti_3C_2T_x$ nanohybrid were obtained to confirm the formation of the $NiCo_2O_4$–$Ti_3C_2T_x$ nanohybrid, and are demonstrated in Fig. 2. After etching out Al from Ti_3AlC_2 (MAX phase), the peak at 9.2° corresponding to the (002) plane in Ti_3AlC_2 was broadened and shifted towards a lower 2θ angle at 6.74° in $Ti_3C_2T_x$ NSs. Furthermore, the distinctive peak for Al vanished (2θ = 39°), signifying the successful etching of Al from the MAX phase to form $Ti_3C_2T_x$ NSs (Fig. S1, ESI†). These findings strongly indicate the formation of $Ti_3C_2T_x$ NSs.[34] The PXRD pattern of $NiCo_2O_4$ NPs (green) exhibited *hkl* planes of (311), (400), (511) and (440) of $NiCo_2O_4$ (JCPDS:00-002-1074).[35] The prominent peak of $Ti_3C_2T_x$ NSs related to the (002) plane is constrained in the $NiCo_2O_4$–$Ti_3C_2T_x$ nanohybrid (blue), which could be due to the minimal amount of MXene used for nanohybrid synthesis. The peaks corresponding to $NiCo_2O_4$ appeared in the PXRD patterns of the $NiCo_2O_4$–$Ti_3C_2T_x$ nanohybrid, which clearly indicates the successful formation of the nanohybrid.

Additionally, HRTEM with SAED and FESEM investigation with elemental mapping were performed to probe the morphology of Ti_3AlC_2, $Ti_3C_2T_x$ NSs, $NiCo_2O_4$ and the $NiCo_2O_4$–$Ti_3C_2T_x$ nanohybrid. The FESEM image of Ti_3AlC_2 (Fig. S2a, ESI†) exhibits a packed layered structure, while $Ti_3C_2T_x$ MXene demonstrates a single nanosheet like morphology (Fig. S2b, ESI†). The FESEM image displayed in Fig. S2c (ESI†) indicates the formation of $NiCo_2O_4$ NPs. Furthermore, the FESEM image of the $NiCo_2O_4$–$Ti_3C_2T_x$ nanohybrid[36] (Fig. S2d, ESI†) clearly indicates the *in situ* formation of $NiCo_2O_4$ NPs on $Ti_3C_2T_x$ NSs. Elemental mapping (Fig. S3, ESI†) reveals the uniform distribution of $NiCo_2O_4$ NPs embedded over $Ti_3C_2T_x$ NSs, with all the elements present in nanohybrid. The TEM images of the *in situ* grown $NiCo_2O_4$ NPs over $Ti_3C_2T_x$ NSs are shown in Fig. 3a and b. Fig. 3a demonstrates the uniform distribution of $NiCo_2O_4$ NPs over the $Ti_3C_2T_x$ NSs and the average size of the $NiCo_2O_4$ NPs is found to be around 12 nm. The TEM image of the prepared $NiCo_2O_4$–$Ti_3C_2T_x$ nanohybrid in Fig. 3b indicates the presence of both the $NiCo_2O_4$ NPs and thin $Ti_3C_2T_x$ MXene NSs. In Fig. 3c, the HRTEM image of $NiCo_2O_4$–$Ti_3C_2T_x$ nanosheets clearly exhibits *d*-spacings of 0.43 and 0.26 nm, corresponding to (002) and (311) planes of $Ti_3C_2T_x$ MXene and spinel $NiCo_2O_4$ NPs, respectively. The SAED pattern (Fig. 3d) reveals well-defined rings that correspond to the crystal planes of the $NiCo_2O_4$ NPs, which are well indexed to (311), (220), and (440).

The XPS survey spectrum (Fig. 4a) of the as synthesized nanohybrid confirmed the existence of Ti, C, Ni, Co and O. In Fig. 4b the Ni 2p spectrum of $NiCo_2O_4$–$Ti_3C_2T_x$ MXene exhibits two binding energy states at 871.45 eV and 853.44 eV and satellite peaks at 878.82 eV and 859.86 eV are associated with Ni 2p3/2 and Ni 2p1/2, respectively.[37] The high resolution spectrum of Co 2p (Fig. 4c) exhibits two peaks that are in agreement with Co 2p3/2 and Co 2p1/2. The binding energy values obtained for $NiCo_2O_4$–$Ti_3C_2T_x$ NSs at 795.45 eV and 780.06 eV are attributed to Co^{2+} and those observed at 793.54 eV and 778.17 eV are ascribed to Co^{3+}. Furthermore, the peaks observed at 798.99 eV and 784.81 eV correspond to satellite peaks.[38] Fig. 4d shows the core level spectrum of Ti in the $NiCo_2O_4$–$Ti_3C_2T_x$ nanohybrid. The presence of titanium carbide and titanium oxide in the nanohybrid could be ascertained from the peaks observed in the Ti 2p state, wherein the peaks at 457.65 and 463.34 eV correspond to Ti–C, and those at 459.41 and 464.51 eV correspond to Ti–O. Ti displays different valence states due to the surface terminal groups like –OH and –F introduced during the etching process. In the C 1s spectrum (Fig. 4e), the binding energies at 280.17 eV and 283.5 eV are assigned to C–Ti and C–C species, and the peaks appearing at 284.82 eV and 286.97 eV are due to C–O and O–C=O bonds.[39,40] Similarly, the O 1s spectrum was fitted over three subpeaks and presented in Fig. 4f. The peak observed at 528 eV correlated well with M–O (Ni–O, Ti–O and Co–O). Furthermore, the concordant peak for –OH on MXene and observed water molecules appeared at the binding energy values of 529.3 eV and 531.1 eV, respectively.[33] The results observed from XPS revealed the presence of Ni and Co in the nanohybrid with +2 and +3 oxidation states, respectively. All these morphological and spectral investigations show that $NiCo_2O_4$ NPs have been uniformly distributed on the $Ti_3C_2T_x$ NSs and the *in situ* growth of $NiCo_2O_4$ NPs over $Ti_3C_2T_x$ NSs would suitably modulate the electronic structure of the nanohybrid. This in turn would facilitate the electrochemical characteristics of the $NiCo_2O_4$–$Ti_3C_2T_x$ nanohybrid modified electrode and its electrocatalytic activity towards Glu and H_2O_2 determination.

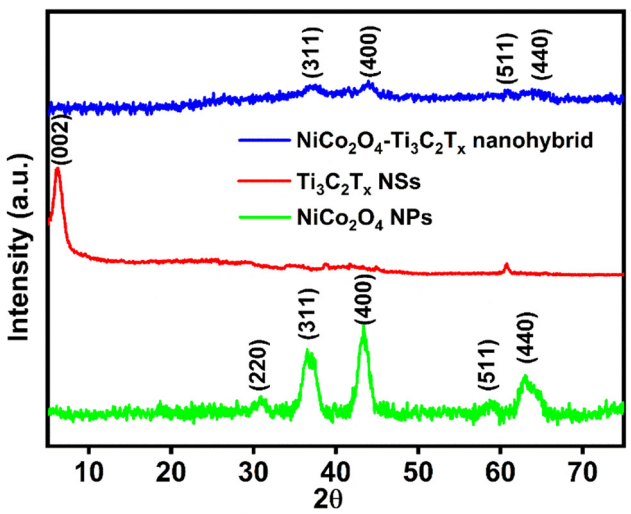

Fig. 2 PXRD patterns of $NiCo_2O_4$ NPs (green), $Ti_3C_2T_x$ NSs (red) and the $NiCo_2O_4$–$Ti_3C_2T_x$ nanohybrid (blue).

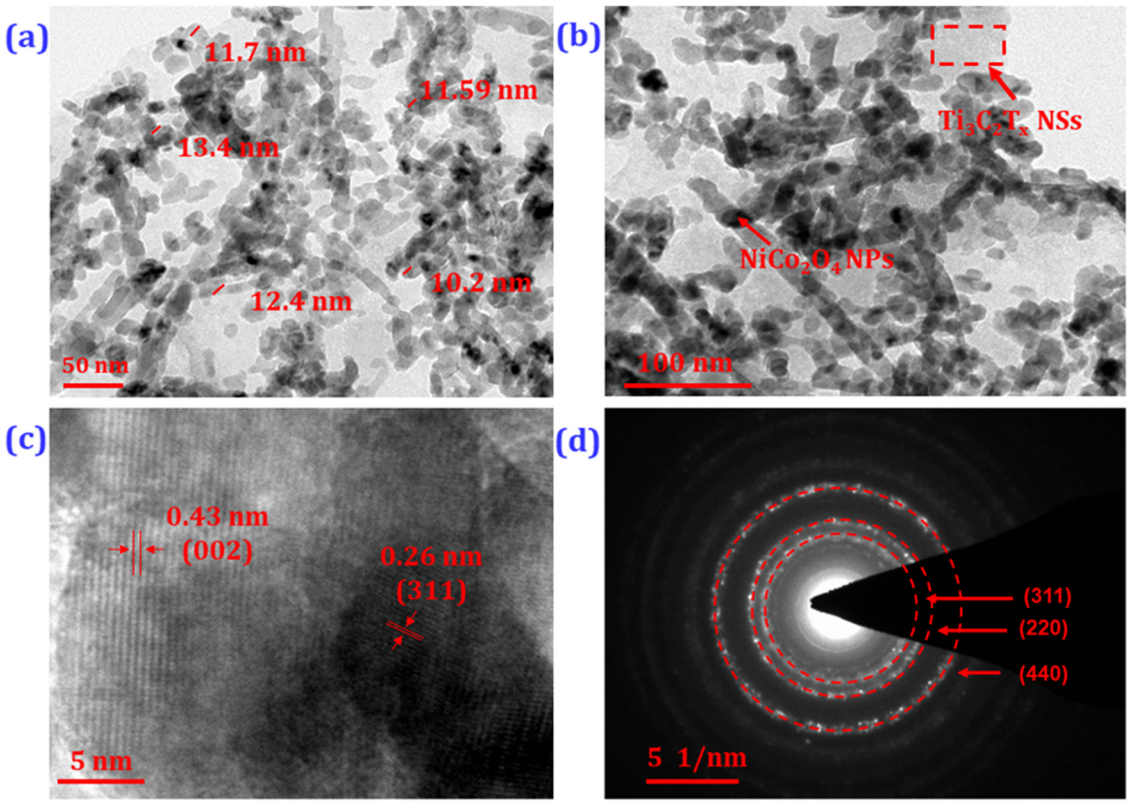

Fig. 3 (a) and (b) TEM images of the $NiCo_2O_4$–$Ti_3C_2T_x$ nanohybrid. (c) and (d) HRTEM image and SAED patterns of the $NiCo_2O_4$–$Ti_3C_2T_x$ nanohybrid.

3.2. Electrochemical behaviour of the $NiCo_2O_4$–$Ti_3C_2T_x$ nanohybrid modified electrode

To assess the electrochemical characteristics of the fabricated $NiCo_2O_4$–$Ti_3C_2T_x$/GCE, cyclic voltammetry (CV) was carried out in 0.1 M NaOH electrolyte at a scan rate of 20 mV s^{-1} within the potential range of +0.2 V to +0.7 V as illustrated in Fig. 5a. The $NiCo_2O_4$–$Ti_3C_2T_x$/GCE exhibited distinct redox peaks, with an anodic peak potential (E_{pa}) observed at +0.56 V and a cathodic peak potential (E_{pc}) at +0.38 V with E° of +0.47 V. The modified electrode prepared in the absence of MXene, *i.e.*, $NiCo_2O_4$/GCE, exhibited redox peaks with E_{pa} and E_{pc} of 0.58 V and 0.42 V with E° of −0.5 V. The obtained well-defined redox peaks are due to the faradaic response of Ni^{3+}/Ni^{2+} and Co^{3+}/Co^{2+} present in the $NiCo_2O_4$ NPs.[41] Notably, the $NiCo_2O_4$–$Ti_3C_2T_x$ nanohybrid modified electrode exhibits lower redox potentials with higher anodic and cathodic peak currents than the original $NiCo_2O_4$ redox spinel oxide NPs. The enhanced electrochemical performance in the case of $NiCo_2O_4$–$Ti_3C_2T_x$/GCE could be due to the 2D MXene NSs that afford higher surface area and also a platform for the uniformly grown $NiCo_2O_4$ NPs (without any aggregation). This heterostructure results in the generation of abundant catalytic sites and is expected to trigger the electrocatalytic activity of the modified electrode. Conversely, the bare and MXene modified GCE exhibited no discernible redox behaviour in the investigated potential window.

An investigation on the effect of scan rate was conducted to examine the nature of the electrochemical process that occurs at the fabricated $NiCo_2O_4$–$Ti_3C_2T_x$/GCE (Fig. S5a, ESI†). As the scan rate increased, the peak currents for both oxidation and reduction gradually increased. As shown in Fig. S5b (ESI†), a linear relationship was obtained for the plot of the square root of scan rate *vs.* peak current, which reveals that the redox process is diffusion-controlled. Additionally, we further planned to examine the number of catalytically active sites by calculating the electrochemical active surface area (ECSA). The ECSA was calculated using the Randles–Sevcik equation (eqn (1)) by investigating the effect of the scan rate of the modified electrode in 5 mM $K_3Fe(CN)_6$.[41]

$$i_p = 2.69 \times 10^5 \times A \times C \times n^{3/2} \times D^{1/2} \times \nu^{1/2} \quad (1)$$

where i_p represents the anodic peak current, A is the ECSA, C refers to the concentration of $K_3Fe(CN)_6$, D is the diffusion coefficient of $K_3Fe(CN)_6$, n refers to the number of electrons involved in the redox reaction and ν is the scan rate. The ECSA values were calculated for $Ti_3C_2T_x$/GCE, $NiCo_2O_4$/GCE and $NiCo_2O_4$–$Ti_3C_2T_x$/GCE, and found to be 0.094, 0.162 and 0.462 cm^2. The remarkably higher ECSA value obtained with $NiCo_2O_4$–$Ti_3C_2T_x$/GCE demonstrates that a larger number of catalytically active sites are being generated upon the formation of the $NiCo_2O_4$–$Ti_3C_2T_x$ heterostructure.

The influence of pH on the electrochemical behaviour of $NiCo_2O_4$–$Ti_3C_2T_x$/GCE was tested in the pH range from 3 to 13 to optimize the working conditions (Fig. S4, ESI†). As observed from the figure, no redox peaks could be obtained in the pH range from 3 to 9, whereas a small oxidation peak was observed at pH 11. However, well-defined redox peaks corresponding to

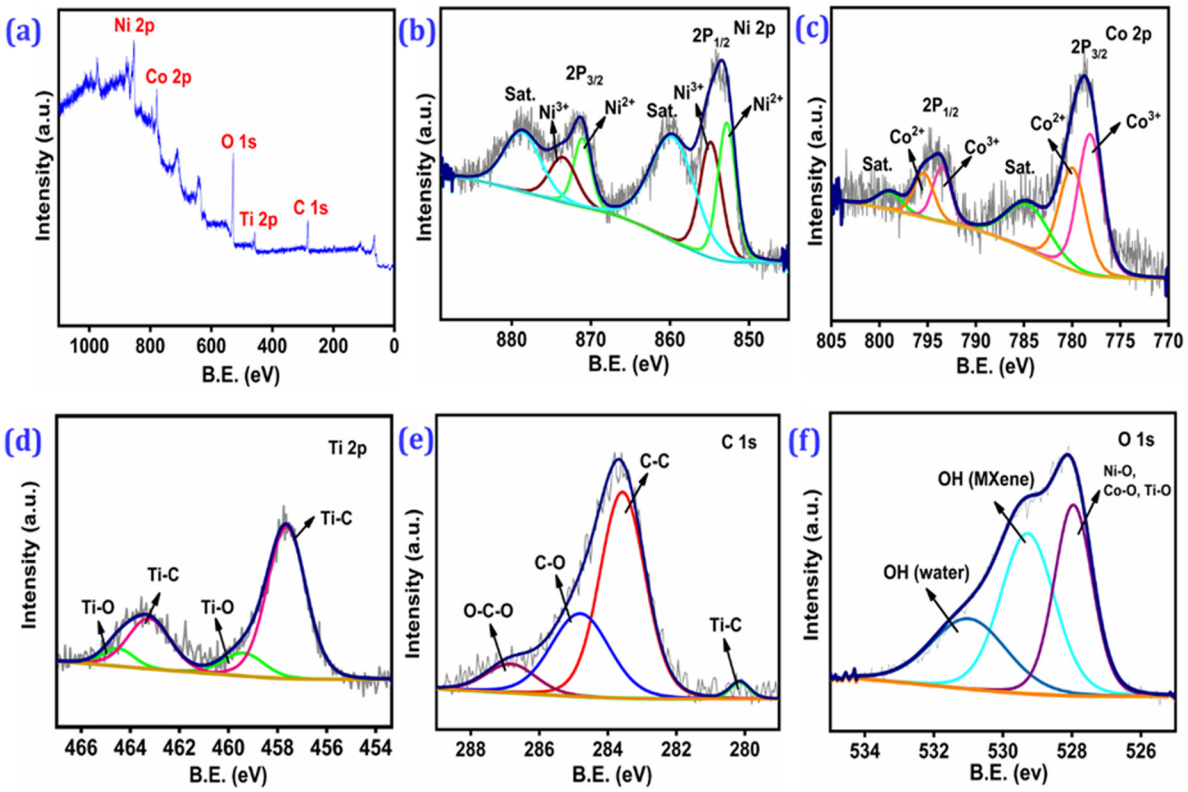

Fig. 4 (a) Survey spectrum of the $NiCo_2O_4$–$Ti_3C_2T_x$ nanohybrid. Core level spectra of (b) Ni 2p, (c) Co 2p, (d) Ti 2p, (e) C 1s, and (f) O 1s in the $NiCo_2O_4$–$Ti_3C_2T_x$ nanohybrid.

Ni^{3+}/Ni^{2+} and Co^{3+}/Co^{2+} could be observed when the pH was further increased to 13 (eqn (2)). No change in the redox response was observed when the pH was increased beyond 13 and hence pH 13 was chosen as the optimum pH for all the electrochemical measurements.

3.3. $NiCo_2O_4$–$Ti_3C_2T_x$ modified electrode towards glucose detection

3.3.1. Investigation of the electrocatalytic performance. As $NiCo_2O_4$–$Ti_3C_2T_x$/GCE has demonstrated distinct electrochemical characteristics, we planned to explore its electrocatalytic activity towards the detection of Glu. The electrocatalytic activity was systematically explored towards Glu detection by recording the CV response of bare-GCE (inset), MXene-GCE (inset), $NiCo_2O_4$/GCE and $NiCo_2O_4$–$Ti_3C_2T_x$/GCE in the presence and absence of Glu as depicted in Fig. 5a. The bare-GCE and $Ti_3C_2T_x$/GCE did not exhibit any catalytic response, whereas the $NiCo_2O_4$/GCE showed a slight but negligible response towards Glu oxidation. Conversely, the $NiCo_2O_4$–$Ti_3C_2T_x$/GCE displayed a noticeable increase in the anodic current around 0.55 V upon the addition of 150 μM Glu. Interestingly, upon injections of Glu in 50 μM increments, a linear enhancement in the anodic peak current was observed, demonstrating the electrocatalytic oxidation of Glu on the surface of $NiCo_2O_4$–$Ti_3C_2T_x$/GCE (Fig. 5b). The enhanced electrocatalytic performance of $NiCo_2O_4$–$Ti_3C_2T_x$/GCE could arise from the intrinsic properties of redox-active $NiCo_2O_4$ spinel metal oxides and high number of active sites and excellent conductivity of the 2D MXene sheets. At an applied potential of 0.5 V, the Ni^{2+} and Co^{2+} ions in the $NiCo_2O_4$ will be electrochemically oxidized to Ni^{3+} and Co^{3+} (eqn (2)). Upon addition of glucose, these metal ions in the oxidized form in turn will oxidize the glucose to gluconolactone and will be reduced to the Ni^{2+} and Co^{2+} states (eqn (3)). Both these reactions (eqn (2) and (3)) will continue in a cycle as long as glucose is available at the electrode surface, which results in an enhanced oxidation current, and this indicates the mediated electrocatalytic oxidation of glucose.[42]

$$NiCo_2O_4 + H_2O + OH^- \rightarrow NiOOH + 2CoOOH + e^- \quad (2)$$

$$Ni^{3+} + Co^{3+} + \text{Glucose} \rightarrow Ni^{2+} + Co^{2+} + \text{Gluconolactone} \quad (3)$$

3.3.2. Amperometric detection of glucose. The impressive catalytic response obtained with $NiCo_2O_4$–$Ti_3C_2T_x$/GCE motivated us to substantiate the catalytic activity towards Glu oxidation under dynamic conditions. Thus, the amperometric response (Fig. 5c) was measured for $NiCo_2O_4$/GCE and $NiCo_2O_4$–$Ti_3C_2T_x$/GCE in 0.1 M NaOH by applying an optimized potential of +0.5 V and dynamic conditions (350 revolutions per minute). The amperometric (i–t) curve is presented in Fig. 5c, wherein the $NiCo_2O_4$–$Ti_3C_2T_x$/GCE responded swiftly to every spike of Glu addition over the linear range of 30 μM to 1.83 mM. The estimated LOD and sensitivity of the fabricated $NiCo_2O_4$–$Ti_3C_2T_x$/GCE based non-enzymatic sensor were calculated to be

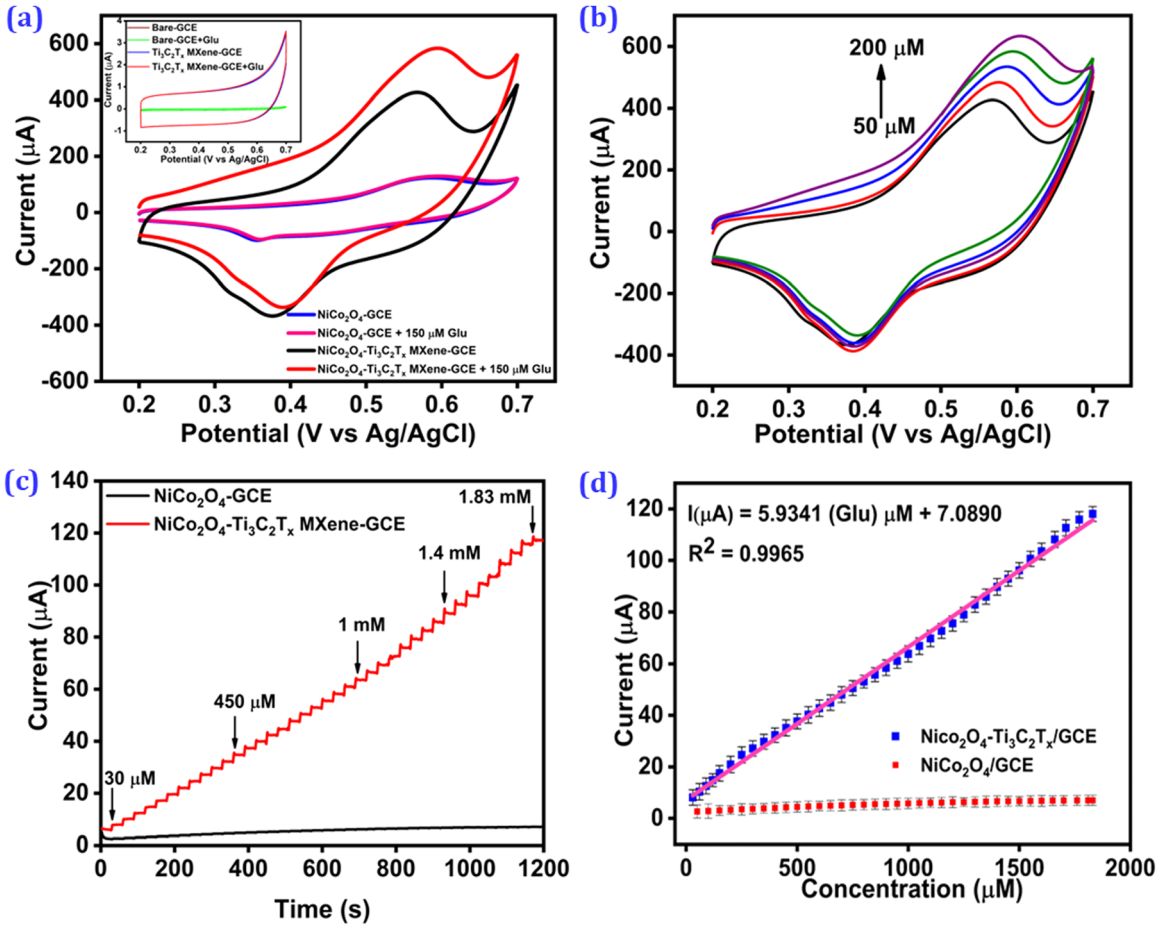

Fig. 5 (a) CVs of the $NiCo_2O_4$/GCE and $NiCo_2O_4$–$Ti_3C_2T_x$/GCE in the presence and absence of 150 μM Glu. Inset: CVs of the unmodified GCE and $Ti_3C_2T_x$/GCE in the presence and absence of 150 μM Glu. (b) CVs of the $NiCo_2O_4$–$Ti_3C_2T_x$/GCE with increasing addition of Glu at 20 mV s^{-1}. (c) Amperometric response of $NiCo_2O_4$/GCE and $NiCo_2O_4$–$Ti_3C_2T_x$/GCE for the successive spikes of Glu in 0.1 M NaOH. (d) Corresponding calibration plots.

9 μM and 101.2 mA μM^{-1} cm^{-2}, respectively. It could also be observed from Fig. 5d that the $NiCo_2O_4$–$Ti_3C_2T_x$/GCE demonstrated remarkably improved current response and catalytic activity compared to those of $NiCo_2O_4$/GCE. The obtained electrochemical performance of $NiCo_2O_4$–$Ti_3C_2T_x$/GCE in terms of low LOD, high sensitivity and wide detection ranges is comparable or better than that of the recently reported non-enzymatic sensors for Glu detection (Table S3, ESI†). This significant catalytic activity and enhanced current response attained with $NiCo_2O_4$–$Ti_3C_2T_x$/GCE is attributed to the large surface area afforded by 2D-$Ti_3C_2T_x$ NSs, inherent properties of uniformly distributed $NiCo_2O_4$ NPs on MXenes and the large number of catalytic sites on the $NiCo_2O_4$–$Ti_3C_2T_x$ heterostructure.

3.3.3. Stability and reproducibility. The effectiveness of the produced sensor heavily depends on its operational stability, long term durability and reproducibility. The $NiCo_2O_4$–$Ti_3C_2T_x$/GCE based sensor was subjected to 50 continuous cycles at 20 mV s^{-1} with the potential ranging from +0.2 V to +0.7 V. The results demonstrated that the sensor was extremely stable with no discernible changes to the anodic and cathodic peak potentials as well as peak currents. The long-term performance of the designed sensor was tested over a period of 30 days with and without 0.05 mM Glu. The sensor maintained 96% of the response in the absence of Glu and 93% of the response while 0.05 mM Glu was present, as represented in the inset of Fig. 6c. These results indicate that the constructed sensor $NiCo_2O_4$–$Ti_3C_2T_x$/GCE has excellent operational consistency and long-term durability for the detection of Glu. Additionally, five identically modified sensors were prepared and used to evaluate the repeatability of the synthetic procedure of $NiCo_2O_4$–$Ti_3C_2T_x$/GCE. A reproducible current response was achieved at the sensors, in the presence and absence of Glu with relative standard deviations (RSD) of 1.86 and 1.56, respectively, as illustrated in Fig. 6d. The results establish firmly that the constructed $NiCo_2O_4$–$Ti_3C_2T_x$/GCE sensors also display good electrode-to-electrode repeatability.

3.3.4. Interference and real sample analysis. To examine the selectivity of the developed sensor for the real time electrochemical detection of Glu, the effect due to interference has been examined by employing amperometry in 0.1 M NaOH at +0.5 V. Fig. 6a illustrates the amperometric detection response of $NiCo_2O_4$–$Ti_3C_2T_x$/GCE for the detection of 20 μM Glu in the presence of 10 times higher concentrations of other coexisting biomolecules, including ascorbic acid (AA), dopamine (DA),

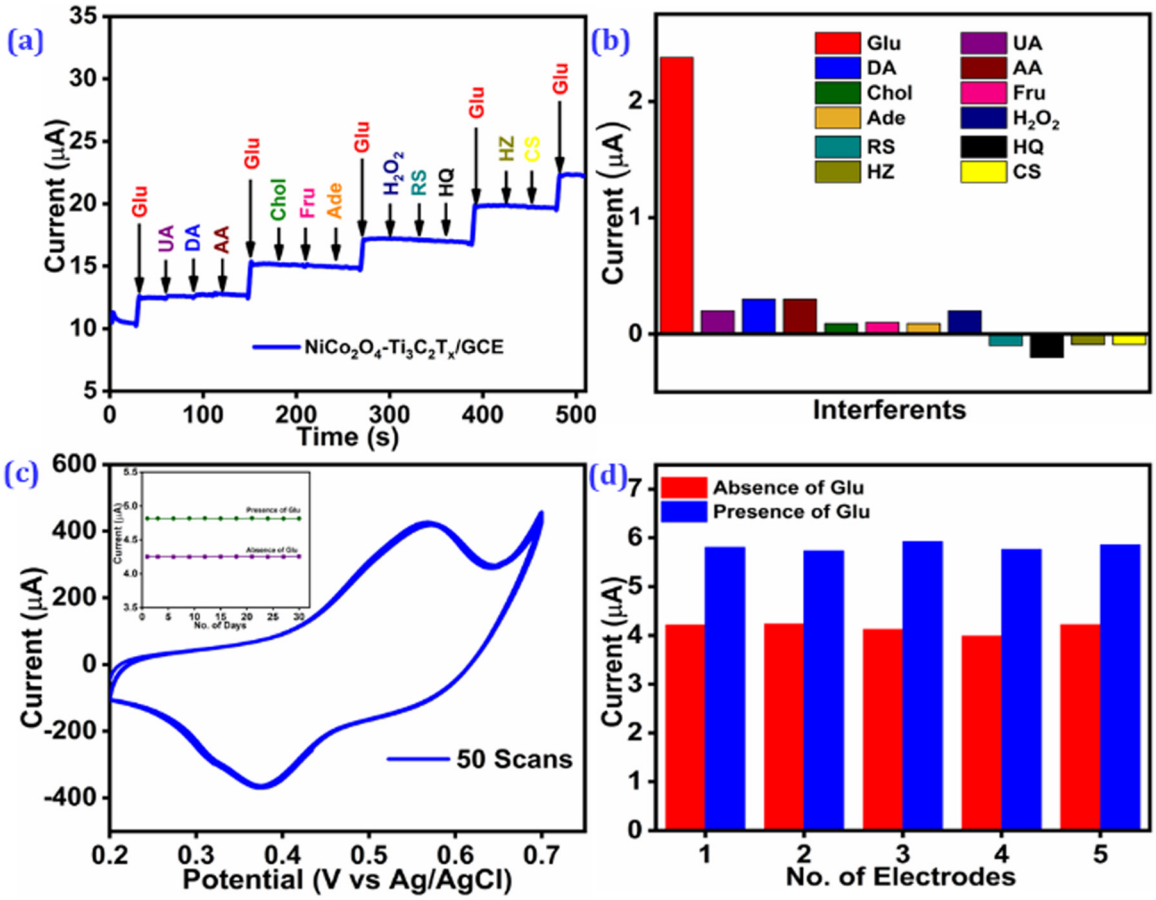

Fig. 6 (a) Interference effect towards Glu detection (20 μM) in the presence of various interfering analytes (0.2 mM) in 0.1 M NaOH. (b) Corresponding bar diagram. (c) Stability investigation for 50 continuous cycles. Inset: Long-term stability of the fabricated sensor for 30 days in the presence and absence of 50 μM Glu. (d) Bar diagram corresponding to the current response in the presence and absence of Glu (50 μM) for five identically prepared sensors.

uric acid (UA), cholesterol (Chol), fructose (Fru), adenine (Ade), H_2O_2, resorcinol (RS), hydroquinone (HQ), hydrazine (HZ), and cysteine (CyS). The bar graph of the corresponding catalytic current in Fig. 6b reveals that the fabricated non-enzymatic sensor did not show significant interference and exhibited high selectivity towards Glu. The applicability of the developed sensor for real time application has been examined by monitoring Glu in serum and urine samples (human). In a typical procedure, a known amount of Glu was spiked into a real sample, and the recovery was obtained from amperometry. The non-enzymatic detection of Glu using the $NiCo_2O_4$–$Ti_3C_2T_x$ nanohybrid decorated GCE resulted in a recovery range of 97.6% to 100.8%, as shown in Table S1 (ESI†). These findings showed the suitability of the constructed system for Glu detection in a biological medium owing to the selectivity and sensitivity acquired from the rationale design of the non-enzymatic sensor by decorating $NiCo_2O_4$ over highly conducting MXene.

3.4. $NiCo_2O_4$–$Ti_3C_2T_x$ modified electrode towards detection of H_2O_2

3.4.1. Investigation of the electrocatalytic performance. The ability of the $NiCo_2O_4$–$Ti_3C_2T_x$ nanohybrid modified electrode to efficiently detect Glu allowed us to envisage the development of a non-enzymatic sensor for the electrochemical detection of H_2O_2. Thus, the electrochemical behaviours of the constructed electrode $NiCo_2O_4$–$Ti_3C_2T_x$/GCE towards H_2O_2 sensing were investigated by recording CV responses in the absence and presence of the analyte in the potential range from 0 V to −0.6 V at a sweep rate of 20 mV s^{-1} in N_2 saturated 0.1 M NaOH. No redox peaks were observed for any of the electrodes in the applied potential range in the absence of H_2O_2. The electrocatalytic activities of the fabricated sensors including bare/GCE, $Ti_3C_2T_x$/GCE, $NiCo_2O_4$/GCE, and $NiCo_2O_4$–$Ti_3C_2T_x$/GCE were studied in the presence of 50 μM H_2O_2. No change in the voltammetric behaviour could be observed for bare/GCE, $Ti_3C_2T_x$/GCE, or $NiCo_2O_4$/GCE in the absence and presence of the analyte, indicating that these electrodes are catalytically inactive. Interestingly, the hybrid nanomaterial $NiCo_2O_4$–$Ti_3C_2T_x$ decorated electrode displayed an increase in the cathodic current around −0.25 V in the presence of 50 μM H_2O_2 and the catalytic current was found to vary linearly with the increase in the concentration of added H_2O_2. These results clearly demonstrate that the electrocatalytic activity towards the reduction of H_2O_2 occurs only at the $NiCo_2O_4$–$Ti_3C_2T_x$/GCE owing to the presence of a catalytically active heterostructure. At the applied potential (−0.25 V), the metal ions would already exist in the reduced form. Upon addition of H_2O_2, these metal

ions will reduce H_2O_2 to H_2O (eqn (4)), and they are oxidized to Ni^{3+} and Co^{3+}, which again will be electrochemically reduced at a potential of −0.25 V to Ni^{2+} and Co^{2+} (eqn (5)). This results in an enhanced reduction current of ∼−0.25 V, corresponding to the $NiCo_2O_4$ mediated electrocatalytic reduction of H_2O_2.[43]

$$Ni^{2+} + Co^{2+} + H_2O_2 + 2H^+ \rightarrow Ni^{3+} + Co^{3+} + 2H_2O \quad (4)$$

$$Ni^{3+} + 2Co^{3+} + 3e^- \rightarrow Ni^{2+} + 2Co^{2+} + 2H_2O \quad (5)$$

3.4.2. Amperometric detection of H_2O_2. The electrochemical performance of the nanohybrid loaded GCE was investigated using amperometry under dynamic conditions. An applied potential of −0.25 V was used as the CVs of $NiCo_2O_4$–$Ti_3C_2T_x$/GCE demonstrated high cathodic peak current at this potential. Fig. 7c exhibits typical amperometric (*i*–*t*) curves of $NiCo_2O_4$/GCE and $NiCo_2O_4$–$Ti_3C_2T_x$/GCE upon sequential addition of H_2O_2 in N_2 saturated 0.1 M NaOH electrolyte solution. The current response obtained for both the modified electrodes gradually decreased for each addition of H_2O_2. A comparatively poor response with no linear variation in current was obtained for $NiCo_2O_4$/GCE. Notably, the $NiCo_2O_4$–$Ti_3C_2T_x$/GCE exhibited a sharp response for every addition of H_2O_2. Linearity was observed in two concentration ranges of 20 to 100 μM and 100 μM to 2.01 mM with sensitivities of 57.2 μA μM^{-1} cm^{-2} and 107.03 μA μM^{-1} cm^{-2}, respectively, and the sensor achieved a LOD of 6 μM. The outcomes are comparable with or even superior to those of the recently published non-enzymatic sensors towards H_2O_2 reduction (Table S3, ESI†). The steady-state current was rapidly achieved within 3s during the electrocatalytic reduction of H_2O_2 at $NiCo_2O_4$–$Ti_3C_2T_x$/GCE. The analytical characteristics obtained in the absence of any enzyme make it obvious that the proposed sensor functions as a robust H_2O_2 sensing platform.

3.4.3. Stability and reproducibility. The stability of the $NiCo_2O_4$–$Ti_3C_2T_x$/GCE non-enzymatic sensor was assessed by measuring its CV response at a scan rate of 20 mV s^{-1} for 50 continuous potential cycles in NaOH (0.1 M; N_2 saturated), which is presented in Fig. 8c. The modified sensor shows good stability for 50 cycles with no noticeable change in potential and current response. In addition, the non-enzymatic sensor was tested over 30 days towards the detection of 0.05 mM H_2O_2. As seen in the inset of Fig. 8c, the biosensor demonstrated an acceptable long-term stability, retaining its activity up to 96.2% and 95.7% for 30 days, when recorded without and with H_2O_2. Additionally, the replicability of the sensor was studied by

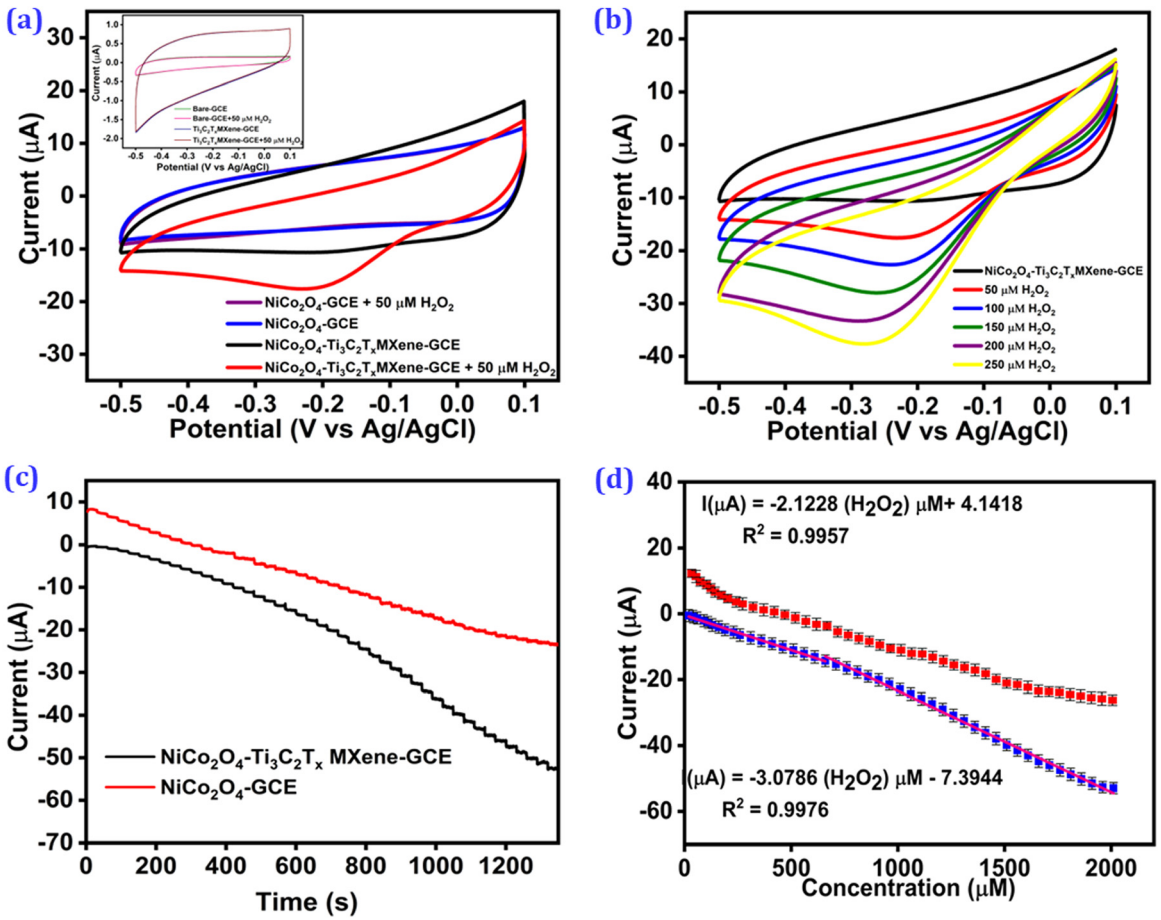

Fig. 7 (a) CVs of the $NiCo_2O_4$/GCE and $NiCo_2O_4$–$Ti_3C_2T_x$/GCE in the presence and absence of 50 μM H_2O_2. Inset: CVs of the unmodified GCE and $Ti_3C_2T_x$/GCE in the presence and absence of 50 μM H_2O_2. (b) CVs of the $NiCo_2O_4$–$Ti_3C_2T_x$/GCE with increasing additions of H_2O_2 at 20 mV s^{-1}. (c) Amperometric response of the $NiCo_2O_4$/GCE and $NiCo_2O_4$–$Ti_3C_2T_x$/GCE for successive spikes of H_2O_2 in N_2 saturated 0.1 M NaOH. (d) Corresponding calibration plots.

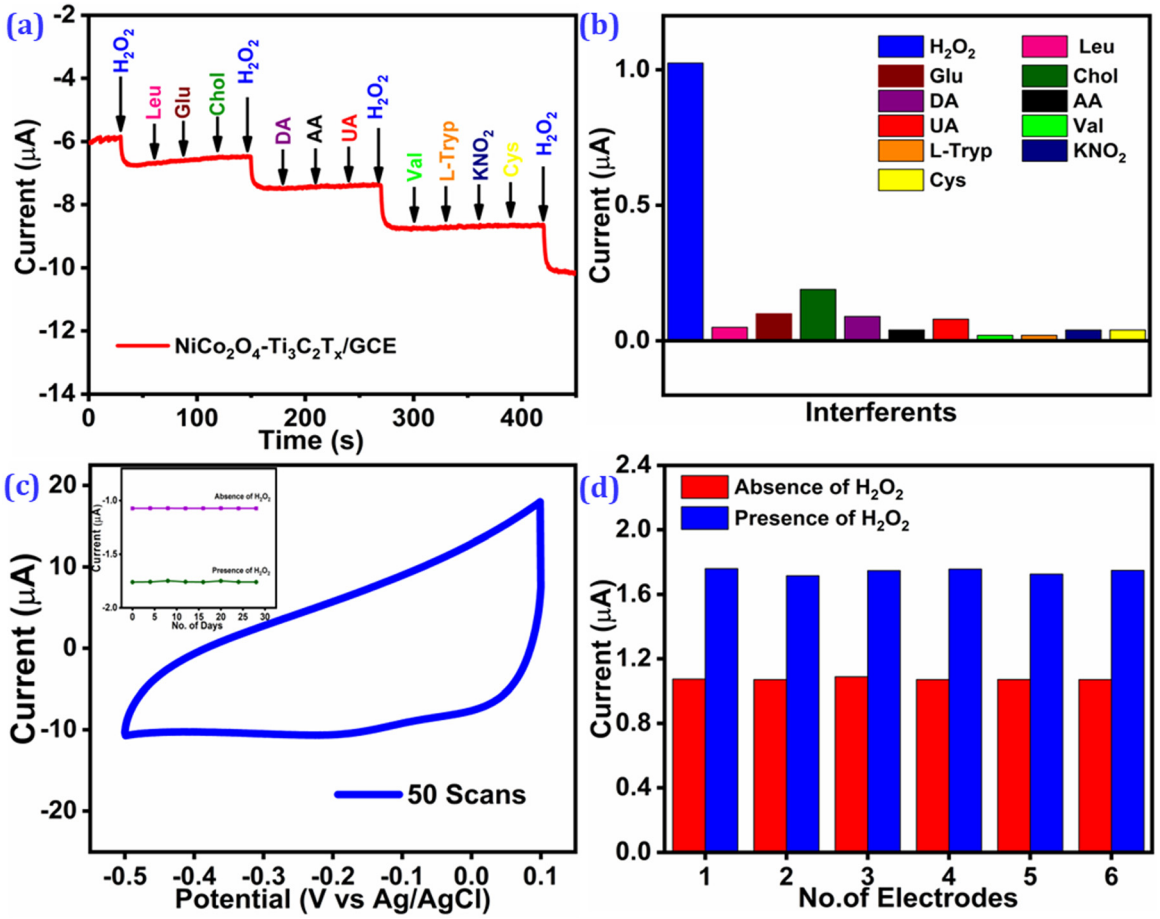

Fig. 8 (a) Interference effect toward H_2O_2 detection (20 μM) in the presence of various interfering analytes (0.2 mM) in N_2 saturated 0.1 M NaOH. (b) Corresponding bar diagram. (c) Stability investigation for 50 continuous cycles. Inset: Long-term stability of the fabricated sensor for 30 days in the presence and absence of 50 μM H_2O_2. (d) Bar diagram corresponding to the current response in the presence and absence of H_2O_2 (50 μM) for five identically prepared sensors.

fabricating 5 different $NiCo_2O_4$–$Ti_3C_2T_x$/GCE sensors, and their electrocatalytic efficacy was investigated towards 0.02 mM H_2O_2. A RSD of 2.8% was detected across the individual electrodes, establishing the good electrode-to-electrode electrocatalytic performance replicability (Fig. 8d). High stability and good reproducibility of the developed non-enzymatic sensor is achieved due to the judicious uniform growth of $NiCo_2O_4$ on the large surface of the MXene NSs.

3.4.4. Interference and real sample analysis. The selectivity of the modified non-enzymatic sensor was evaluated by adding 0.2 mM of interfering species, including Leu, L-tryp, Chol, Val, KNO_2, Cys, Glu, AA, DA and UA along with 20 μM H_2O_2. The investigation was carried out amperometrically at an applied potential of −0.25 V. Fig. 8a illustrates that even in the presence of ten times greater concentration of these interfering species, the current response did not change significantly and only the addition of H_2O_2 produced a notable current response. The observed outcomes indicate that the $NiCo_2O_4$–$Ti_3C_2T_x$/GCE has an acceptable selectivity for determination of H_2O_2. As H_2O_2 is commonly used as a preservative in food products, in this work, the applicability of $NiCo_2O_4$–$Ti_3C_2T_x$/GCE has been assessed by detecting H_2O_2 in milk and apple juice samples. By employing a conventional addition method, known amounts of H_2O_2 were injected to apple juice and milk samples and amperometry was used to determine their recovery at an operating potential of −0.25 V. The results (Table S2, ESI†) demonstrated recoveries ranging from 97.8 to 105.6%, indicating that the fabricated H_2O_2 sensor has the ability to detect the analyte in complex real samples.

4. Conclusion

The $NiCo_2O_4$–$Ti_3C_2T_x$ nanohybrid was rationally designed and utilized towards the fabrication of a facile electrochemical sensor for the detection of glucose and H_2O_2. The $NiCo_2O_4$–$Ti_3C_2T_x$/GCE sensor demonstrated good electrocatalytic activity along with good selectivity, remarkable stability and reproducibility. The inherent catalytic properties of $NiCo_2O_4$ NPs, augmented conductivity of $Ti_3C_2T_x$ NSs and increased number of catalytically active sites due to the $NiCo_2O_4$–$Ti_3C_2T_x$ heterostructure collectively result in promising analytical performance of the sensor. Furthermore, the practical applicability of the developed sensor for H_2O_2 and Glu was tested using food

(milk and apple juice) and biological samples (serum and urine), respectively, and it exhibited satisfactory recovery results. As a result, the fabricated sensor could be potentially utilized for medical diagnosis and environmental monitoring. With the increase in the development of a wide variety of 2D materials, many of novel high-performing nanohybrids and heterostructures could be designed not only for sensor design, but also for other task specific applications.

Author contributions

Devarasu Mohanapriya: conceptualization, methodology, investigation, validation, writing – original draft. Kathavarayan Thenmozhi: conceptualization, resources, supervision, project administration, writing – review & editing.

Data availability

The data supporting this article have been included as part of the ESI.† The original files will be made available on request.

Conflicts of interest

There are no conflicts to declare.

Acknowledgements

The authors acknowledge the Central Research Facilities (CRF), Vellore Institute of Technology (VIT) for providing instrumentation facilities.

Notes and references

1 S. Arora, R. Nagpal, M. Gusain, B. Singh, Y. Pan, D. Yadav, I. Ahmed, V. Kumar and B. Parshad, *ACS Sens.*, 2023, **8**, 443–464.
2 C. D. Flynn, D. Chang, A. Mahmud, H. Yousefi, J. Das, K. T. Riordan, E. H. Sargent and S. O. Kelley, *Nat. Rev. Bioeng.*, 2023, **1**, 560–575.
3 C. Lino, S. Barrias, R. Chaves, F. Adega, P. Martins-Lopes and J. R. Fernandes, *Biochim. Biophys. Acta, Rev. Cancer*, 2022, 1877.
4 Y. Zhu, J. Qian, K. Xu, W. Ouyang, J. Yang and N. Yang, *Chem. Eng. J.*, 2024, **485**, 149795.
5 S. M. Ismail, A. A. Abd-Elaal, F. H. Abd El-salam, F. A. Taher, I. Aiad and S. M. Shaban, *Chem. Eng. J.*, 2022, 139593.
6 H. Teymourian, A. Barfidokht and J. Wang, *Chem. Soc. Rev.*, 2020, **49**, 7671–7709.
7 K. Theyagarajan, B. A. Lakshmi, C. Kim and Y. J. Kim, *Mater. Today Chem.*, 2024, **41**, 102282.
8 T. Elshaarani, H. Yu, L. Wang, Z. Zain-Ul-Abdin, R. S. Ullah, M. Haroon, R. U. Khan, S. Fahad, A. Khan, A. Nazir, M. Usman and K. U. R. Naveed, *J. Mater. Chem. B*, 2018, **6**, 3831–3854.
9 P. Manusha, K. Theyagarajan, M. Elancheziyan, H. Shankar, K. Thenmozhi and S. Senthilkumar, *ECS Sens. Plus*, 2022, **1**, 033601.
10 V. P. Sruthi and S. Senthilkumar, *J. Mater. Chem. C*, 2024, **12**, 8924–8934.
11 G. He, F. Gao, W. Li, P. Li, X. Zhang, H. Yin, B. Yang, Y. Liu and S. Zhang, *Anal. Methods*, 2019, **11**, 1651–1656.
12 H. Dong, L. Zhao, T. Wang, Y. Chen, W. Hao, Z. Zhang, Y. Hao, C. Zhang, X. Wei, Y. Zhang, Y. Zhou and M. Xu, *Anal. Chem.*, 2023, **95**, 8340–8347.
13 Y. Li, L. Luo, Y. Kong, Y. Li, Q. Wang, M. Wang, Y. Li, A. Davenport and B. Li, *Biosens. Bioelectron.*, 2024, 249.
14 M. Song, L. Dang, J. Long and C. Hu, *ACS Sens.*, 2018, **3**, 2518–2525.
15 X. Qiao, Y. Cai, Z. Kong, Z. Xu and X. Luo, *ACS Sens.*, 2023, **8**, 2834–2842.
16 C. Zhu, G. Yang, H. Li, D. Du and Y. Lin, *Anal. Chem.*, 2015, **87**, 230–249.
17 Y. Xie, T. Liu, Z. Chu and W. Jin, *J. Electroanal. Chem.*, 2021, 893.
18 M. Govindaraj, A. Srivastava, M. K. Muthukumaran, P. C. Tsai, Y. C. Lin, B. K. Raja, J. Rajendran, V. K. Ponnusamy and J. Arockia Selvi, *Int. J. Biol. Macromol.*, 2023, **253**, 126680.
19 H. Zhu, L. Li, W. Zhou, Z. Shao and X. Chen, *J. Mater. Chem. B*, 2016, **4**, 7333–7349.
20 H. Yin, Y. H. Shi, Y. P. Dong and X. F. Chu, *J. Electroanal. Chem.*, 2021, **885**, 115100.
21 S. M. Babulal, S. M. Chen, R. Palani, K. Venkatesh, A. S. Haidyrah, S. K. Ramaraj, C. C. Yang and C. Karuppiah, *Colloids Surf., A*, 2021, **621**, 126600.
22 Y. Feng, D. Xiang, Y. Qiu, L. Li, Y. Li, K. Wu and L. Zhu, *Electroanalysis*, 2020, **32**, 571–580.
23 A. Chen, Y. Wei, D. Tuo, C. Zhou, S. Shi, N. Tang, Q. He and J. Liu, *J. Alloys Compd.*, 2023, **970**, 172557.
24 J. Zhao, Y. Long, C. He, H. Yang, S. Zhao, X. Luo, D. Huo and C. Hou, *ACS Sustainable Chem. Eng.*, 2023, **11**, 2160–2171.
25 M. Y. Emran, A. Kotb, A. B. Ganganboina, A. Okamoto, T. Z. Abolibda, H. A. H. Alzahrani, S. M. Gomha, C. Ma, M. Zhou and M. A. Shenashen, *Anal. Chim. Acta*, 2024, 342985.
26 M. Naguib, V. N. Mochalin, M. W. Barsoum and Y. Gogotsi, *Adv. Mater.*, 2014, **26**, 992–1005.
27 Y. Gogotsi and B. Anasori, *ACS Nano*, 2019, **13**, 8491–8494.
28 P. A. Shinde, A. M. Patil, S. Lee, E. Jung and S. Chan Jun, *J. Mater. Chem. A*, 2022, **10**, 1105–1149.
29 Y. Zhong, R. Liao, G. He, S. Liu, J. Zhang and C. Chen, *Microchim. Acta*, 2024, **191**, 572.
30 D. Mohanapriya, J. Satija, S. Senthilkumar, V. Kumar Ponnusamy and K. Thenmozhi, *Coord. Chem. Rev.*, 2024, 507.
31 Y. Shao, Y. Zhu, R. Zheng, P. Wang, Z. Zhao and J. An, *Adv. Compos. Hybrid Mater.*, 2022, **5**, 3104–3116.
32 A. Vahidmohammadi, J. Moncada, H. Chen, E. Kayali, J. Orangi, C. A. Carrero and M. Beidaghi, *J. Mater. Chem. A*, 2018, **6**, 22123–22133.
33 D. U. Lee, B. J. Kim and Z. Chen, *J. Mater. Chem. A*, 2013, **1**, 4754–4762.
34 M. Alhabeb, K. Maleski, B. Anasori, P. Lelyukh, L. Clark, S. Sin and Y. Gogotsi, *Chem. Mater.*, 2017, **29**, 7633–7644.

35 S. Gupta, S. Tiwari, V. K. Arghode and G. Deo, *Energy Fuels*, 2024, **38**, 11022–11036.
36 M. Naguib, M. Kurtoglu, V. Presser, J. Lu, J. Niu, M. Heon, L. Hultman, Y. Gogotsi and M. W. Barsoum, *Adv. Mater.*, 2011, **23**, 4248–4253.
37 N. Narayanan, H. Liu, W. Zhang, B. Ravichandran, Q. Xu, L. Khotseng, Y. Cheng and H. Su, *ACS Appl. Nano Mater.*, 2024, **7**, 3907–3917.
38 W. Wang, G. Chen, W. Kong, J. Chen, L. Pu, J. Gong, H. Zhang and Y. Dai, *J. Energy Storage*, 2024, **86**, 111097.
39 X. Lu, J. Zhu, W. Wu and B. Zhang, *Electrochim. Acta*, 2017, **228**, 282–289.
40 S. Li, L. Zhao, J. Shu, H. Niu, R. Li, J. Zhao, H. Yang, J. Jin and R. Jin, *J. Colloid Interface Sci.*, 2022, **610**, 944–952.
41 Md. Z. Kabira, C. Erkmena, S. Kurbanoglua, G. A. Tigb and B. Uslu, *J. Electroanal. Chem.*, 2023, **994**, 117651.
42 P. S. Shewale and K. S. Yun, *Heliyon*, 2023, **6**, 17200.
43 J. Jiang, Z. Zhang, C. Yang, R. Wang and Z. Wu, *RSC Adv.*, 2022, **12**, 35199–35205.

